AIP | Journal of
Renewable and Sustainable Energy

Lift and drag characteristics of a cascade of flat plates in a configuration of interest for a tidal current energy converter: Numerical simulations analysis

D. Cebrián, J. Ortega-Casanova, and R. Fernandez-Feria

Citation: J. Renewable Sustainable Energy **5**, 043114 (2013); doi: 10.1063/1.4816495
View online: http://dx.doi.org/10.1063/1.4816495
View Table of Contents: http://jrse.aip.org/resource/1/JRSEBH/v5/i4
Published by the AIP Publishing LLC.

JOURNAL OF RENEWABLE AND SUSTAINABLE ENERGY **5**, 043114 (2013)

Lift and drag characteristics of a cascade of flat plates in a configuration of interest for a tidal current energy converter: Numerical simulations analysis

D. Cebrián, J. Ortega-Casanova, and R. Fernandez-Feria[a)]
E. T. S. Ingeniería Industrial, Universidad de Málaga, Dr Ortiz Ramos s/n,
29071 Málaga, Spain

(Received 7 February 2013; accepted 10 July 2013; published online 23 July 2013)

Numerical simulations of the three-dimensional flow through a cascade of flat plates are conducted to analyze its lift and drag characteristics in a configuration of interest for a particular type of tidal hydrokinetic energy converter. To that end, the turbulent model parameters in the computational fluid dynamics code are validated against experimental data for the flow around an isolated plate at different angles of incidence and the same Reynolds number used in the cascade. The lift and drag coefficients of a plate in the cascade, as well as the effective nondimensional power extracted from the tidal current, are compared to the corresponding values for an isolated plate. These results are used as a guide for the design of the optimum configuration of the cascade (angle of attack, blade speed, and solidity) which extracts the maximum power from a tidal current for a given reference value of the Reynolds number. © *2013 AIP Publishing LLC*. [http://dx.doi.org/10.1063/1.4816495]

I. INTRODUCTION

The conversion of the kinetic energy of tidal or river currents into electricity is currently made by different types of turbines and non-turbine systems.[1,2] Given that tidal hydrokinetic energy has the potential to play a valuable part in a sustainable energy future,[2,3] it is not surprising that much research effort is undertaken in many countries to generate new and more efficient devices to extract kinetic energy from tidal currents, both by improving existing turbines or by devising new ones. In both cases, fundamental and applied researches are needed to improve the energy efficiency of the new devices and to reduce their environmental impact. In this context, a Norwegian company has developed a new non-turbine device consisting of a cascade of underwater sails or blades that travel carried by the tidal current in a given direction, which in turn drive an electric generator.[4] This device has the potential for a great extraction efficiency, posing some fundamental hydrodynamic problems about the lift and drag characteristics of a cascade of moving sails or blades in a particular configuration in relation to the tidal or river current. This is the problem undertaken in this work. For simplicity is restricted here to a cascade of flat plates moving perpendicularly to the tidal current, which is one of the configurations of greatest interest.[4] Three-dimensional numerical simulations of the flow around this array of plates with a given aspect ratio and for a given characteristic value of the Reynolds number are used to compute the lift and drag coefficients of the plates. The resulting power coefficients are used to find out the optimal configuration in terms of the blades angle of attack, speed, and separation or solidity. Although no other detailed hydrodynamic numerical study for the optimization of the hydrokinetic energy converter considered here has been made so far, there exists in the literature analogous investigations based on both two- and three-dimensional

---

[a)]Electronic mail: ramon.fernandez@uma.es numerical simulations aimed at the optimization of the hydrodynamic performance of several types of marine current turbines (see, e.g., Refs. 5–7).

The physical problem is formulated in Sec. II. The numerical model used in the computational fluid dynamics (CFD) simulations is discussed in Sec. III, where the turbulent parameters in the model and the computational grid are validated against existing experimental data for a single plate at different angles of attack. The numerical results for different configurations of the cascade of flat plates are given in Sec. IV, including a discussion of the flow configuration yielding optimal power efficiency. Finally, the main conclusions are drawn in Sec. V.

II. FORMULATION OF THE PROBLEM

We consider the incompressible flow of a uniform (tidal or river) current of velocity $\mathbf{V}$ through a cascade of rectangular flat plates of chord length c and height b moving at a velocity $\mathbf{U}$ perpendicular to the current $\mathbf{V}$ (see Fig. 1(a)). The separation between the parallel plates is s and their incidence (stagger) angle γ. For the numerical simulations it is convenient to use a reference frame moving with the plates in which the x axis coincides with the direction of the relative velocity $\mathbf{W}$ (Fig. 1(b)). In this reference frame, the effective angle of attack in relation to the relative velocity is $\alpha = \gamma - \theta$, where θ is the angle between the current velocity $\mathbf{V}$ and the relative velocity $\mathbf{W}$.

The Reynolds number based on the current speed $V(\equiv |\mathbf{V}|)$ and the chord length c,

$$Re = \frac{Vc}{\nu}\,, \tag{1}$$

where ν is the kinematic viscosity, will be fixed in all the numerical simulations to a characteristic value (see Sec. III). For this given Re, we shall analyze the effect that the cascade speed U, the separation between plates s, and the stagger angle γ (or angle of attack α) have on the power extracted from the current. That is, we shall vary the non-dimensional parameters γ,

$$\xi \equiv \frac{U}{V} = \tan\theta\,, \quad \text{and} \quad \sigma \equiv \frac{c}{s}\,, \tag{2}$$

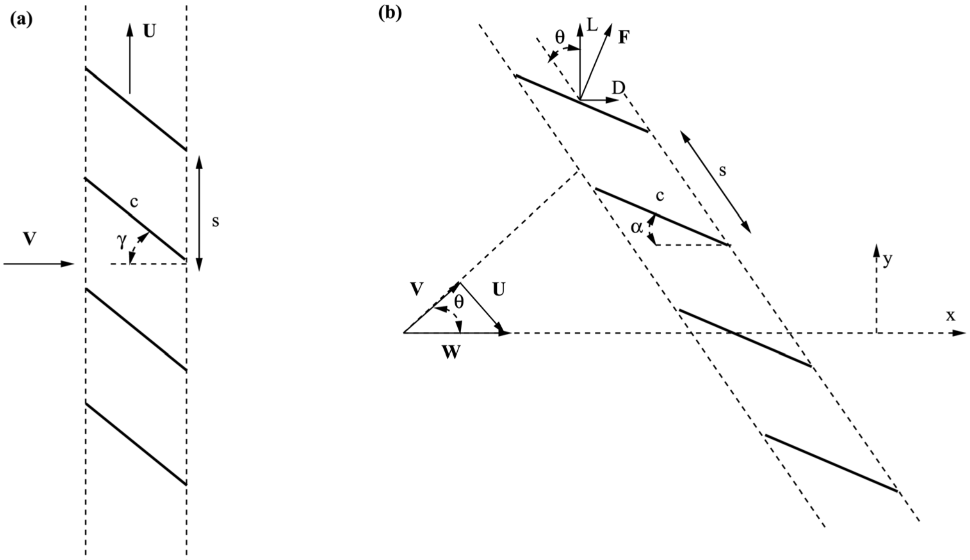

FIG. 1. Sketch of the cascade of flat plates moving perpendicularly to the incident current **V** (a) and in the reference frame where the plates are steady and the relative velocity **W** is in the x-direction (b).

to find out the values of these parameters that maximize the power extracted from the current for a given Re and for the configuration of Fig. 1(a) where the cascade moves perpendicularly to the current.

From a numerical point of view, we shall compute the total (pressure plus viscous) force $\mathbf{F}$ that the fluid exerts on a plate in the cascade when the incident flow speed is W and the angle of attack is α; this force is decomposed in a "lift" component L and "drag" component D (see Fig. 1(b)). The Reynolds number based on W is related to (1) by

$$Re_W \equiv \frac{Wc}{\nu} = \frac{Re}{\cos\theta} = Re\sqrt{1+\xi^2}\,. \tag{3}$$

For given Re_W, ξ, and solidity σ, we shall compute the nondimensional lift and drag coefficients,

$$C_L = \frac{L}{\frac{1}{2}\rho W^2 cb}\,, \qquad C_D = \frac{D}{\frac{1}{2}\rho W^2 cb}\,, \tag{4}$$

where ρ is the fluid density, for increasing values of α. This process will be repeated for different values of ξ (that also modifies Re_W, see Eq. (3)) and σ. At the end, we will be interested on how these parameters affect the effective power extracted to the current, which is proportional to (see Fig. 1(b))

$$P_U = (L\cos\theta - D\sin\theta)U\,. \tag{5}$$

We define the following power coefficient:

$$C_P \equiv \frac{P_U}{\frac{1}{2}\rho V^3 cb} = (C_L - \xi C_D)\xi\sqrt{1+\xi^2}\,, \tag{6}$$

which will be optimized in relation to γ, ξ and σ for given Re and aspect ratio b/c. Note that C_L and C_D will be obtained from the numerical simulations as functions of α for different values of σ and ξ, being

$$\gamma = \alpha + \theta = \alpha + \arctan(\xi)\,. \tag{7}$$

III. EQUATIONS, NUMERICAL CODE, AND ITS VALIDATION AGAINST EXPERIMENTAL RESULTS FOR AN ISOLATED PLATE

The governing equations are the Reynolds-averaged Navier-Stokes equations for an incompressible flow (constant density ρ), which can be written as

$$\nabla\cdot\mathbf{v} = 0, \tag{8}$$

$$\frac{\partial\mathbf{v}}{\partial t} + \nabla\cdot(\mathbf{v}\mathbf{v}) = -\nabla p + \nabla\cdot\left[(\nu+\nu_t)\left(\nabla\mathbf{v} + (\nabla\mathbf{v})^T\right)\right], \tag{9}$$

where $\mathbf{v}$ is the mean velocity field, p the mean kinematic pressure (pressure divided by ρ) field, and ν_t is the kinematic eddy viscosity. For the numerical computations we used the open source CFD software package OPENFOAM®, produced by OpenCFD Ltd,[8] with different two-equation turbulence models to compute ν_t.[9,10]

In particular, we used two different turbulence models: a Re-Normalisation Group (RNG) $k-\epsilon$ model[11] and a Shear Stress Transport (SST) $k-\omega$ model,[12] both implemented in the OPENFOAM toolbox. The turbulence model equations and some numerical details are summarized in the Appendix. To select the best upstream values of the different turbulent variables for the present problem, together with the optimum computational grid, we simulated numerically the three-dimensional (3D) flow around a single flat plate with semispan aspect ratio (SAR) of 3,

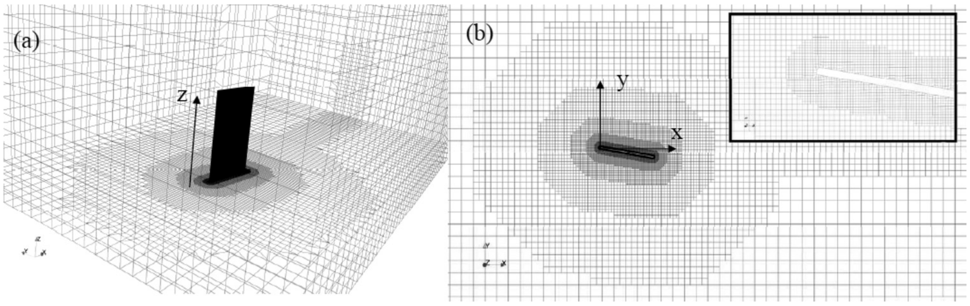

FIG. 2. (a) General view of the computational domain and mesh with 3,300,198 cells used in the computations for the 3D flow around a flat plate with $\mathrm{sAR} = 3$ and angle of incidence $\alpha = 10°$. (b) Plan view of the mesh with a detail of the leading edge of the plate. The dimensions of the computational domain are: $-3c \leq x \leq 7c$, $-c(3 + \sin c) \leq y \leq 3c$, and $0 \leq z \leq 4.5c$.

$Re_W = 8 \times 10^4$ and different angles of attack (see Fig. 2 for the computational domain and mesh). The reasons for selecting this test case were that there exist accurate experimental data for the lift and drag coefficients obtained in a water tunnel by Pelletier and Mueller,[13] and that both the aspect ratio and the Reynolds number are in the range of interest for the tidal flow around the submerged sails in the device that motivated the present study.[4] Smaller values of sAR, between 1 and 3, would also be appropriate. Note that the plane $z = 0$ (Fig. 2) is a symmetry plane in the computational domain, both for the single flat plate and for the cascade, thus reducing to half the number of mesh nodes needed in the numerical computations. This configuration and the plate geometry coincide with those considered experimentally for a single plate in Ref. 13.

The boundary conditions used in the numerical computations are the following: In the inlet section $x = -3c$ (see Fig. 2) a uniform velocity in the x–direction was fixed, given by the selected Reynolds number, together with zero normal gradient (called "slip" condition in the OPENFOAM toolbox) for the pressure and fixed given values for the turbulent parameters. These upstream values of the turbulent parameters were varied to best fit the numerical results (see

TABLE I. Number of mesh cells and upstream values of the turbulence model parameters in each one of the 8 different computational cases considered in Fig. 5 for the flow around a single flat plate (k in $\mathrm{m}^2/\mathrm{s}^2$, ϵ in $\mathrm{m}^2/\mathrm{s}^3$ and ω in s^{-1}). Also included in the last column is the computational time in hours to advance 10^{-1} units of non-dimensional time for $\alpha = 10°$ (see Fig. 4(d)), using just one CPU, and the mean time step Δt (see main text).

Case	Number of Mesh cells	Turbulent model Parameter values	CPU time (h) Δt (s)
1	98 3941	RNG $- k - \epsilon$	42.6
		$k_\infty = 0.0074\,, \epsilon_\infty = 0.032$	10^{-2}
2	33 00198	RNG $- k - \epsilon$	206.8
		$k_\infty = 0.0074\,, \epsilon_\infty = 0.032$	6×10^{-3}
3	33 00198	RNG $- k - \epsilon$	171.4
		$k_\infty = 0.096\,, \epsilon_\infty = 0.00552$	7×10^{-3}
4	52 08203	RNG $- k - \epsilon$	611.6
		$k_\infty = 0.0074\,, \epsilon_\infty = 0.032$	6×10^{-3}
5	98 3941	SST $- k - \omega$	23.0
		$k_\infty = 0.0074\,, \omega_\infty = 0.389$	8.3×10^{-3}
6	33 00198	SST $- k - \omega$	265.9
		$k_\infty = 0.0074\,, \omega_\infty = 0.389$	1.4×10^{-2}
7	33 00198	SST $- k - \omega$	284.5
		$k_\infty = 0.0096\,, \omega_\infty = 0.05175$	7×10^{-3}
8	52 08203	SST $- k - \omega$	563.7
		$k_\infty = 0.0074\,, \omega_\infty = 0.389$	6×10^{-3}

Table I and discussion below). In the outlet section, far downstream the plate ($x = 7c$), the pressure was set constant to its reference value (zero) and "inlet/outlet" conditions were used for the velocity and turbulent parameters. On the upper ($z = 4.5c$) and lateral surfaces (see Fig. 2) slip conditions were used for all the variables, while symmetry conditions were used on the lower surface ($z = 0$) where the flat plate is anchored. Finally, at the solid wall surfaces of the flat plate the velocity was set to zero, a slip condition was used for the pressure, and several specific wall conditions, implemented in the OPENFOAM toolbox and using standard wall functions, were used for k, ϵ, and ω in the different models (see the Appendix for these and other computational details). To generate the computational mesh we used the OPENFOAM "snappyHexMesh" program, with the imported form of the flat plate (see inset in Fig. 2(b)), which was previously generated using MATLAB. To solve the equations, we used the "GAMG—Generalised geometric-algebraic multi-grid" solver for the pressure, and the "smoothSolver" for the remaining variables, both implemented in the OPENFOAM toolbox.[8] They are based on iterative methods for sparse linear systems.[14]

Most of the reported computations were made in a computer cluster with 5 nodes and up to 22 parallel processors managed by the Linux Ubuntu server 10.04. Not all the nodes have the same characteristics, so that there existed a great variety of computational performances when using different combinations of the number of nodes and the number of parallel processors. It suffices to say here that the computation speed for a typical case reported below was increased almost 13 times when using all the 5 nodes with 22 parallel processors, in relation to just one 64-bit processor Intel(R) Core(TM) 2CPU 6600 at 2.66 GHz and 2.99GB of RAM.

To check the accuracy of the numerical results against the experimental data cited above we selected different meshes, and several upstream values of the turbulent kinetic energy (k_∞), dissipation (ϵ_∞), and specific dissipation rate (ω_∞) in the two turbulence models. In particular, for each set of upstream turbulent parameters considered (about five sets for each turbulence model), and for several angles of attack, a grid independent study was conducted using meshes with increasing resolution (see below). The numerical results converged appropriately in most cases, but the agreement of these converged numerical results with the experimental ones depended on the set of turbulent parameters used. To simplify the presentation of this comparison with the experimental results, we report here only 8 different cases, as summarized in Table I: 3 different grids with increasing number of cells, combined with two different sets of parameters for each turbulence model in the case of the "medium" mesh (that depicted in Fig. 2), and only one of the sets of parameters for each turbulence model in the cases of the "coarse" and the "fine" meshes (although all the other upstream turbulence model parameters were also checked with these meshes). The coarse and the fine meshes had a similar distribution of cells in each model but with smaller and larger number of cells, respectively (see Table I). On the other hand, the values of the upstream turbulence model parameters for each set given in Table I correspond to those recommended for each model in the OPENFOAM toolbox[8] for similar 3D aerodynamic flows and Reynolds numbers (cases 3 and 7), and those computed by us using the turbulence intensity and its streamwise variation rate measured in a wind tunnel facility in our laboratory, for the given Reynolds number (remaining cases). Many more values of k_∞, ϵ_∞ and ω_∞ were tested, but we report here only a selection of them, including the cases that best fitted the experimental data for each model. Table I contains also information about the computational time and the time step. At each instant the time step was adjusted to a Courant number of 0.2, and Table I shows the approximately constant values reached after the initial transient.

Some results for $\alpha = 10^\circ$ are shown in Figs. 3 and 4. In particular, Fig. 3 shows the eddy viscosity contours when computed with both turbulence models (cases 2 and 6 in Table I). Note that their values and distributions are quite different, explaining the significant differences in the lift and drag coefficients computed with each model observed below. Figure 4 shows some relevant results when the parameters of case 6 are used: a detail of the final steady state of the non-dimensional streamwise velocity and pressure fields in the vicinity of the flat plate, the final values of the pressure and friction coefficients on the upper and lower surfaces of the plate, and the temporal evolutions of the lift and drag coefficients. The pressure and friction

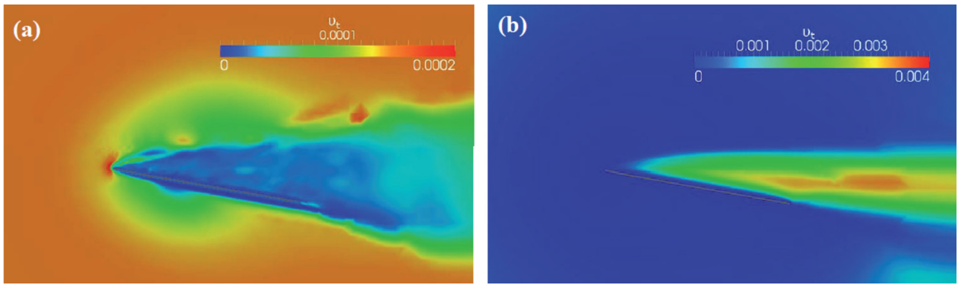

FIG. 3. Contours of the computed eddy viscosity ν_t on a portion of the middle plane $z = 1.5c$ for the 3D flow around a flat plate with sAR $=3$, $Re_W = 8 \times 10^4$ and $\alpha = 10°$ when the RNG $- k - \epsilon$ and the SST $- k - \omega$ turbulence models are used. In particular, (a) corresponds to case 2 in Table I and (b) to case 6.

coefficients, C_p and C_f, are both made dimensionless with $\frac{1}{2}\rho W^2$, and it is observed that C_f is much smaller than C_p. Note also in Fig. 4(d) the oscillations at the initial stages of the numerical simulations, which are due to the fact that the computations started with the flow at rest. However, a steady state was already reached at non-dimensional time $tW/c \simeq 0.40$ (the results plotted in Figs. 4(a)–4(c) are for $t\, W/c = 0.5$).

Figure 5 contains the comparison of the experimental results of Pelletier and Mueller[13] for the lift and drag coefficients as functions of the angle of attack α with the values of C_L and C_D computed numerically with each one of the 8 cases given in Table I. It is clear from this figure that the SST $- k - \omega$ model works much better for this problem than the RNG $- k - \epsilon$ model, especially when the second set of upstream turbulent parameters mentioned above is used. In addition, it is observed that the results obtained with the medium mesh practically coincide with those obtained with the fine mesh. Therefore, we selected the medium mesh, since the computational time and memory are both much smaller than for the fine mesh, together with the SST $- k - \omega$ turbulent model with k_∞ and ω_∞ given by the second set of parameters. That is, we selected the parameters of case 6 in Table I for most of the computations reported below.

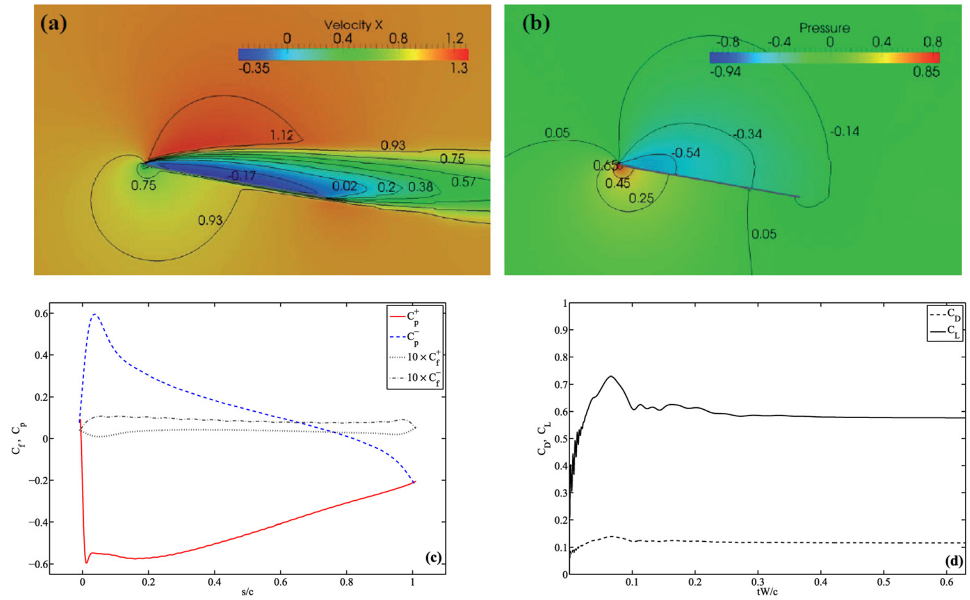

FIG. 4. Plan view of the computed non-dimensional streamwise velocity component (a) and pressure (b) contours on a portion of the middle plane $z = 1.5c$ for the 3D flow around a flat plate with sAR $= 3$, $Re_W = 8 \times 10^4$ and $\alpha = 10°$ when the parameters of case 6 in Table I are used. The results are for the final steady state; the velocity is non-dimensionalized with the incident speed W and the pressure with $\frac{1}{2}\rho W^2$. (c) Distribution of the pressure and friction coefficients, C_p and C_f, on the upper ($^+$) and lower ($^-$) surfaces of the plate for the same time (s is the coordinate along the plate; note that (b) is the distribution of C_p on $z = 1.5c$). (d) Computed temporal evolutions of C_L and C_D.

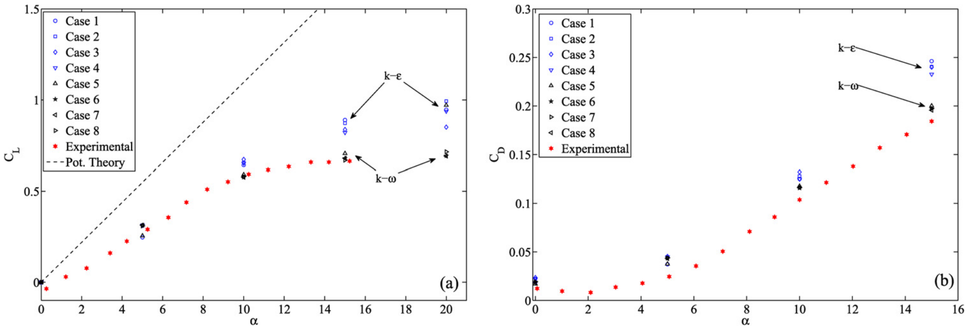

FIG. 5. Comparison between the experimental results of Pelletier and Mueller[13] for C_L (a) and C_D (b) vs. the angle of attack α for a flat plate with sAR = 3 and $Re_W = 8 \times 10^4$ and the numerical results obtained which each one of the 8 cases given in Table I. For reference sake, the potential 2D flow result $C_L = 2\pi \sin \alpha$ is also included in (a).

However, for higher values of the angle of attack than those depicted in Fig. 5 (i.e., $\alpha \gtrsim 20$, for which no previous experimental data exist to compare with), we used the fine mesh in the computations (case 8 in Table I). In fact, to check the accuracy of the numerical results we also calculated the relative errors of each mesh using Richardson extrapolation,[15] in addition to the above comparison with previous experimental results. Particularly, we computed the fourth-order estimate of C_L for each α with Richardson extrapolation using the medium and fine meshes (grid refinement ratio $r \simeq 1.6$; see, e.g., Roache[16] for the details), and with this value estimated the relative errors in C_L when computed with the medium and the fine meshes, respectively, for each α. Table II contains the results. One can observe that for $\alpha = 25^\circ$ and 30° the relative errors estimated for the mean final values of C_L are not sufficiently small when obtained with the medium mesh, while they remain acceptable when using the fine mesh. This is a consequence of the oscillatory behavior of the wake behind the flat plate, due to vortex shedding after flow separation, when the angle of attack $\alpha \gtrsim 20$ (Sec. IV). Therefore, we used the fine mesh in the computations of the flow around a single plate when $\alpha > 20^\circ$, and the medium mesh for $\alpha \leq 20^\circ$.

For a cascade of flat plates, the mesh used in the numerical computations reported below is similar to, and has the same resolution of, the medium one depicted in Fig. 2 for a single plate, but containing several flat plates in a computational domain such that one may set periodic boundary conditions (see Fig. 6). In particular, all the boundary conditions are the same as those described above for the case of a single flat plate, except for the cyclic boundary conditions for all the fluid variables (including the turbulent functions k, ϵ and ω) which are set between the "inclined" surfaces partially seen in the plan view depicted in Fig. 6. We have selected this configuration and domain size, with at least three plates (width $3s$ perpendicular to the cyclic plane, where s is the separation between plates), to simplify the numerical implementation, since it was easier to adjust the number of plates to a fixed periodic domain (sometimes we had to add fractions of a plate) than to change the shape and the size of the computational domain whenever the separation between plates or the angle of attack was varied.

TABLE II. Estimations of the relative errors in the final mean value of C_L for a single plate computed with the medium and fine meshes, in relation to the extrapolated Richardson estimate, for different values of α.

$\alpha(^\circ)$	Error in $C_L(\%)$ 1 plate Medium mesh	Error in $C_L(\%)$ 1 plate Fine mesh
5	1.45	0.36
10	1.00	0.25
15	1.94	0.48
20	4.16	1.04
25	38.81	9.70
30	37.11	9.28

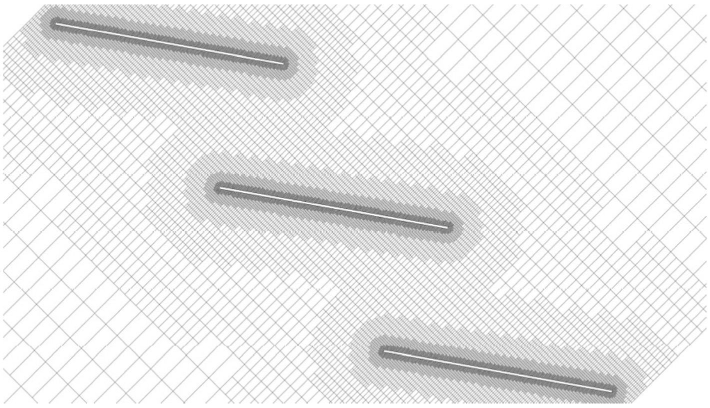

FIG. 6. Plan view (constant z) of a detail of the (medium) computational mesh used in the numerical simulations for the cascade of flat plates with $\xi = U/V = 1\,(\theta = 45^\circ)$, $\sigma = c/s = 1$ and $\alpha = 10^\circ$. It is similar to that depicted in Fig. 2, but with a periodic array of three flat plates. The computational domain is (x along the cyclic plane and y perpendicular to it): $-3c \le x \le 3c$, $0 \le y \le 3s$, $0 \le z \le 4.5c$. The total number of cells is 6,123,575.

To select the appropriate mesh for each angle of attack, we also estimated the relative numerical errors in C_L using Richardson extrapolation with medium and fine meshes (see Table III). Now, the computational errors with the medium mesh were acceptable (much below 10% in most cases) even for high values of the angle of attack, as a consequence of the fact that the flow remains attached to the plates in the cascade (see Sec. IV). Therefore, since the necessary computational time and memory are both much larger with the fine mesh than with the medium mesh, we used the medium one in all the computations reported below for a cascade of flat plates.

IV. RESULTS AND DISCUSSION

We have performed a series of numerical simulations using the numerical code discussed above with the objective of finding out the optimum configuration of the cascade of flat plates that extracts the maximum power from a given tidal current. In particular, we fixed $Re = 5.66 \times 10^4$ (which corresponds to $Re_W = 8 \times 10^4$ for $\xi = 1$) and sAR = 3, as the reference values (like in Sec. III), and looked for the optimum value of α (or γ) which yields the maximum C_P when ξ and σ are varied. These results are compared with the corresponding ones for an isolated flat plate.

The main aerodynamic effect of a cascade in relation to a single blade is that the lift coefficient of each element in the cascade could be substantially increased in relation to the same isolated element if the stagger angle and the separation between blades are conveniently selected, as already predicted from the two-dimensional potential theory of a cascade of flat plates (see, e.g., Weinig;[17] in particular, for $\gamma \to 90^\circ$ and $\sigma \approx 1$, the 2D potential lift tends to infinity).

TABLE III. Estimations of the relative errors in the final mean value of C_L for a plate in a cascade computed with the medium and fine meshes, in relation to the extrapolated Richardson estimate, for different values of α. ($\xi = 1$, $\sigma = 1$, sAR = 3, $Re_W = 8 \times 10^4$).

$\alpha(^\circ)$	Error in $C_L(\%)$ cascade Medium mesh	Error in $C_L(\%)$ cascade Fine mesh
5	2.19	0.55
10	0.59	0.15
15	5.85	1.46
20	0.33	0.08
25	0.27	0.07
30	2.32	0.58

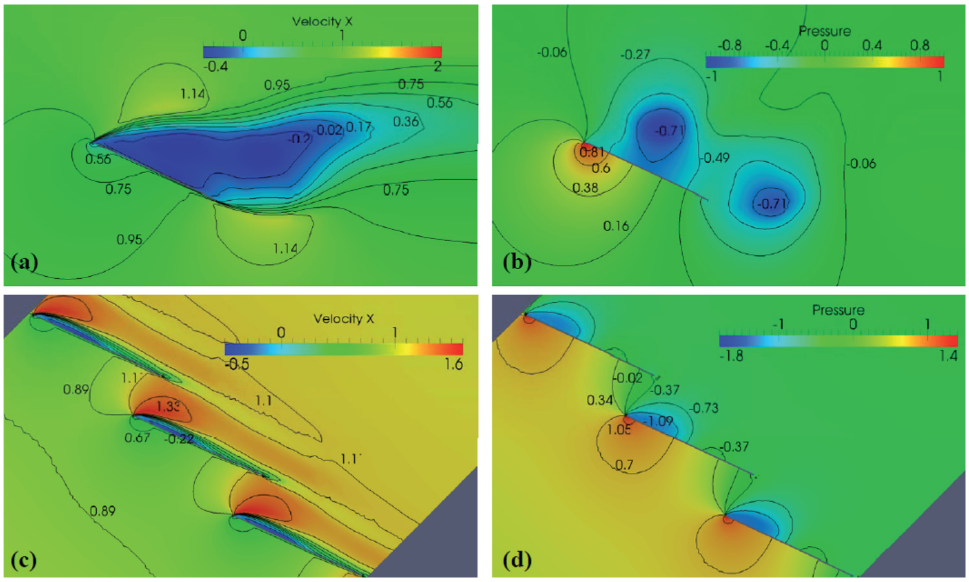

FIG. 7. Plan view of the computed non-dimensional streamwise velocity component and pressure fields (the velocity is scaled with W and the pressure with $\frac{1}{2}\rho W^2$) on a portion of the middle plane $z = 1.5c$ for the 3D flow around a single flat plate (a) and (b), and a cascade with $\sigma = 1$ and $\xi = 1$ (c) and (d), for $\alpha = 25^\circ$ (sAR $= 3$, $Re_W = 8 \times 10^4$).

When viscous and 3D effects are taken into account, this potential increase in the lift coefficient cannot be so pronounced as predicted by the 2D potential theory, but still it may be very significant, mainly due to the "streaming" effect of the cascade, that delays the stall as the angle of attack is increased. Thus, higher lift coefficients can be attained for a plate in a cascade than for an isolated plate when the angle of attack is sufficiently high and the lift of the single plate has already dropped. However, as we shall see, the drag coefficient for the plate in the cascade may be larger than for an isolated plate, and the lift coefficient may be smaller,

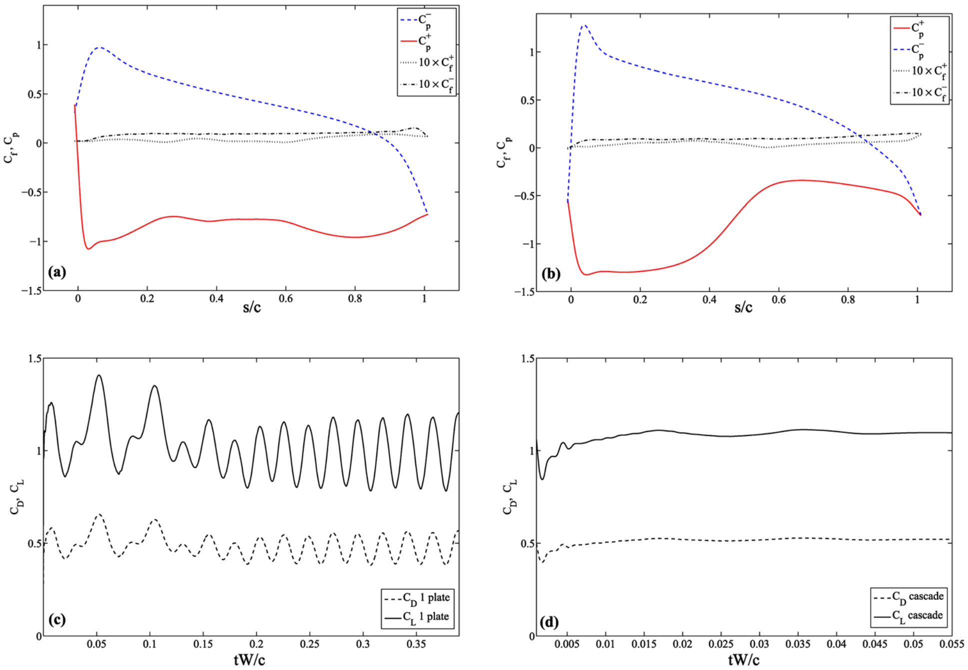

FIG. 8. Distribution of the pressure and friction coefficients, C_p and C_f, on the upper ($^+$) and lower ($^-$) surfaces for an isolated plate (a), and for a plate in the cascade (b), for the same cases of Figs. 7(c) and 7(d) computed temporal evolutions of C_L and C_D for the same cases of Fig. 7.

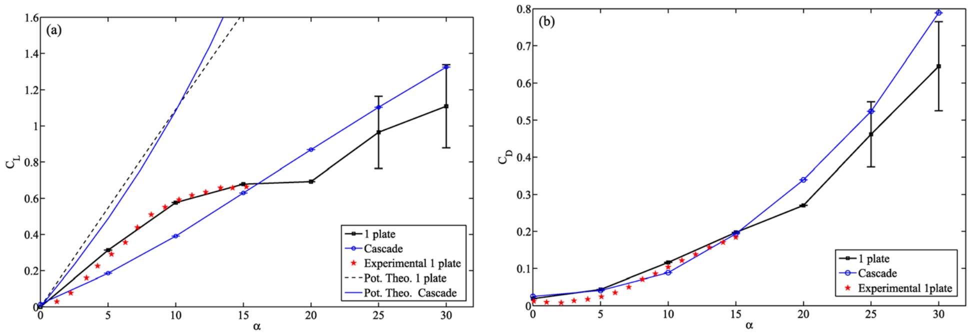

FIG. 9. Comparison between C_L (a) and C_D (b) vs. α for an isolated plate and for a cascade with $\sigma = 1$ and $\xi = 1$ (sAR = 3, $Re_W = 8 \times 10^4$). The error bars indicate the amplitude of the temporal oscillations around their mean values due to the oscillatory wake behind an isolated flat plate. The experimental results for a single plate by Pelletier and Mueller[13] are included. Also included in (a) for reference sake is the 2D potential flow result $C_L = 2\pi \sin\alpha$ for a single plate and the corresponding potential result for a cascade of flat plates.[17]

depending on the particular configuration, so that the global effect of lift and drag coefficients on C_P has to be analyzed for all the different configurations, or different values of γ, ξ and σ.

To illustrate this, Figs. 7 and 8 show a comparison between the velocity and pressure fields around a single plate and through a cascade of flat plates with $\xi = \sigma = 1$ and $\alpha = 25°$. For this angle of attack, the single flat plate is already stalled, and the wake behind it becomes oscillatory due to the vortex shedding, as it is clear in the time evolution of C_D and C_L of Fig. 8(c) (the images in Figs. 7(a) and 7(b) correspond to an instant of time after the permanent oscillatory regime has been reached, and one can clearly identify two vortices in the pressure field picture of Fig. 7(b), which are evolving in time). On the contrary, the flow in the cascade for this high angle of attack is still attached to the plates, with just a narrow region of flow recirculation on the upper surfaces of the plates close to the leading edge. This divergence between the flow regimes in the two configurations starts at a value of α between 15° and 20°, above which the flow over a single plate becomes separated and the mean value of C_L ceases to increase like in the case of a cascade (see Fig. 9). The oscillatory wake is clearly observed for angles of attack α above 25°, approximately, as indicated in Fig. 9 by the error bars attached to the mean values of C_L and C_D for a single plate, which measure the amplitude of the computed oscillations around their mean values. The amplitude of the oscillations in C_L and C_D for an isolated plate is even larger for $\alpha = 30°$ than for $\alpha = 25°$ (see Fig. 10(a)). In contrast, for the cascade, a stationary steady state is always reached for all the values of α considered here (up to $\alpha = 30°$), and C_L keep increasing with α (see Fig. 9(a)). As a consequence, the maximum value of the power coefficient (6) for the cascade (which in the present configuration with $\xi = 1$ is given by $C_P = \sqrt{2}(C_L - C_D)$) is reached at a relatively high value of α, and C_P becomes larger than for an isolated plate (see Fig. 11). It is worth commenting here that although the maximum in the mean value of C_P for an isolated plate is reached in this case for

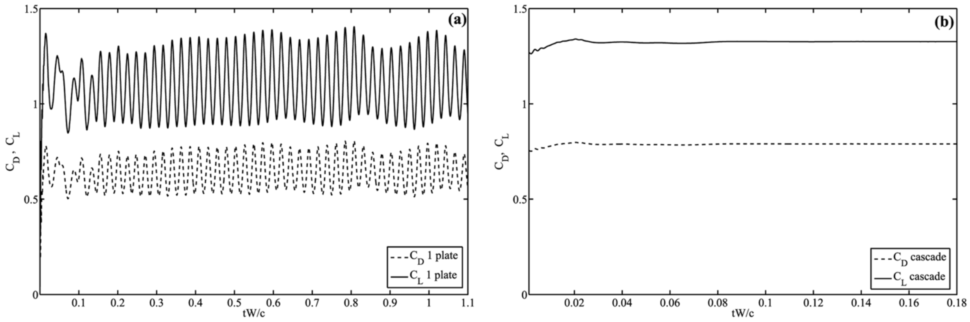

FIG. 10. Computed temporal evolutions of C_L and C_D for the same cases of Fig. 7, but for $\alpha = 30°$.

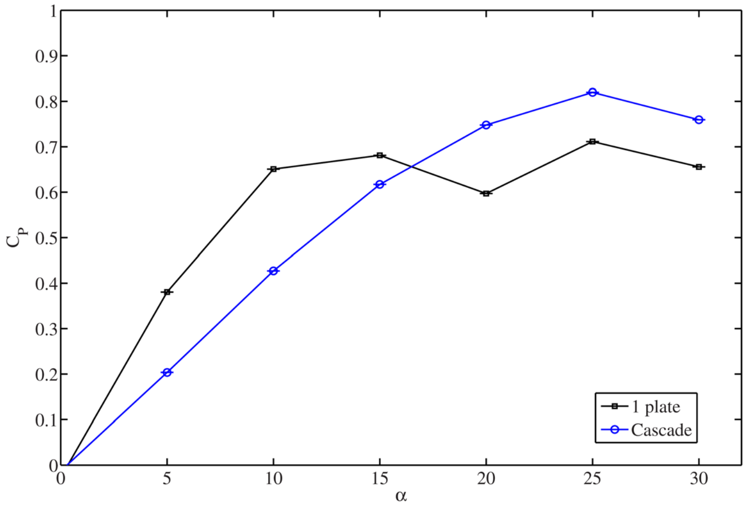

FIG. 11. Comparison between C_P vs. α for an isolated plate and for a cascade with $\sigma = 1$ and $\xi = 1$ (sAR = 3, $Re_W = 8 \times 10^4$). Only the mean values are plotted for the isolated plate.

an angle α in the same range than for a cascade, the large oscillations in C_L and C_D, due to the oscillatory wake behind the plate for these high values of α, make useless this maximum of C_P for an isolated plate from a practical point of view. Thus, the other relative maximum of C_P for a single plate, reached for a smaller value of α (see Fig. 11), is the most interesting one from practical point of view. In either case, this maximum of C_P is, in the present configuration, smaller than that for a plate in a cascade.

This qualitative behavior as the angle of attack is varied is not the general rule for all the values of σ and ξ considered in this work. For instance, for the same $\sigma = 1$ but for larger $\xi = U/V$ (e.g., $\xi = 2.5$, see Fig. 12), the maximum value of C_P is higher for an isolated plate than for a plate in the cascade, and in both cases this maximum is reached for a similar, relatively low, value of the angle of attack α. This is due to the fact that the role of the drag C_D in C_P becomes more important as ξ increases (see (6), and note also in Fig. 1 that the angle θ increases with ξ), so that the maximum of C_P is reached in both cases at low values of α for which C_L for an isolated plate is larger, and so is C_P (see Fig. 12). On the other hand, for $\xi = 1$ and $\sigma \simeq 1.43$ (Fig. 13), which corresponds to a smaller separation s between the plates in

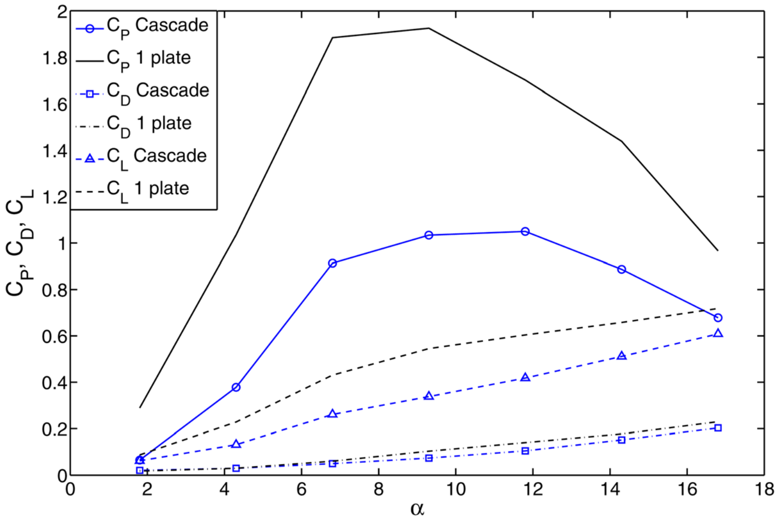

FIG. 12. Comparison between C_P, C_L, and C_D vs. α for an isolated plate and for a cascade with $\sigma = 1$ and $\xi = 2.5$.

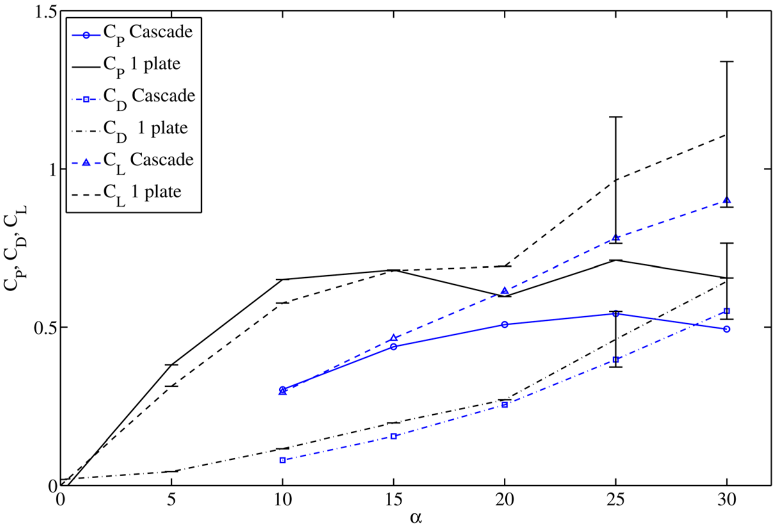

FIG. 13. Comparison between C_P, C_L, and C_D vs. α for an isolated plate and for a cascade with $\sigma \simeq 1.43$ ($\sigma^{-1} = 0.7$) and $\xi = 1$.

the cascade, the situation is qualitatively similar to that depicted in Fig. 11, but now the maximum value of C_P for a single plate is slightly larger than for a plate in the cascade because C_L remains lower in this last case even in the range of values of α where $C_{P,max}$ is reached for the cascade. The reason for this different behavior has to be found in the flow through the cascade, which is shown in Fig. 14 for $\alpha = 25^\circ$, corresponding roughly to the maximum of C_P. Comparing Figs. 14(a) and 14(b) with Figs. 7(c) and 7(d), the main difference is that the recirculation region above the plates is larger when the separation between plates is smaller ($\sigma = 1.43$ in Fig. 14(a)) due to the larger speed between the plates in the cascade. As a

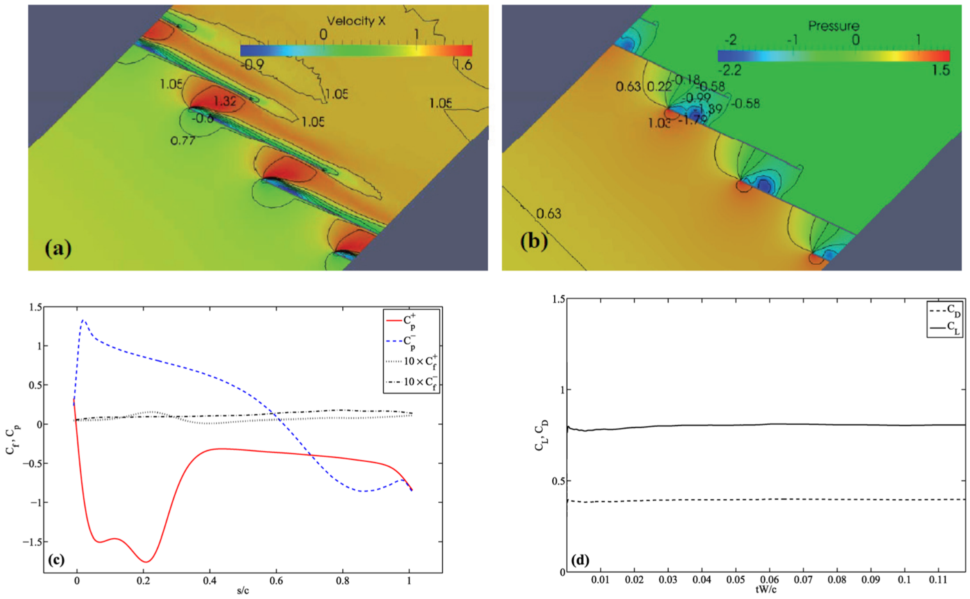

FIG. 14. Plan view of the computed non-dimensional streamwise velocity component (a) and pressure (b) contours on a portion of the middle plane $z = 1.5c$ for the final steady state of the 3D flow through a cascade with $\xi = 1$, $\sigma \simeq 1.43$ and $\alpha = 25^\circ$ (sAR = 3, $Re_W = 8 \times 10^4$). The velocity is non-dimensionalized with W and the pressure with $\frac{1}{2}\rho W^2$. (c) Distribution of the pressure and friction coefficients, C_p and C_f, on the upper ($^+$) and lower ($^-$) surfaces of a plate in the cascade for the same time (s is the coordinate along the plate, $z = 1.5c$). (d) Computed temporal evolutions of C_L and C_D for a plate in the cascade.

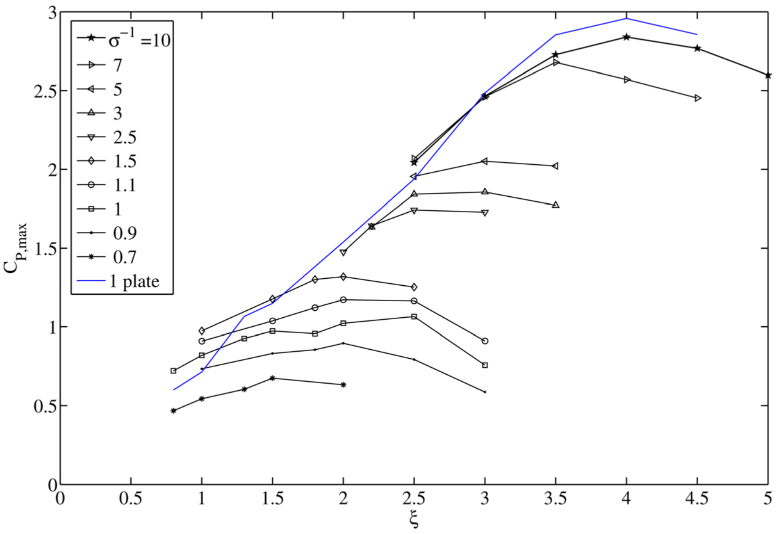

FIG. 15. $C_{P,max}$ as a function of ξ for different values of σ^{-1}. Also included is the curve for a single plate as a function of ξ. (sAR = 3, $Re_W = 8 \times 10^4$.)

consequence, the lift coefficient is smaller than for $\sigma = 1$ (compare Fig. 8(d) with Fig. 14(d)), and so it is $C_{P,max}$.

Figure 15 summarizes $C_{P,max}$ for all the values of ξ and σ considered in this work. In particular, curves of $C_{P,max}$ as functions of ξ are plotted for different values of the solidity σ (in fact, the non-dimensional plate separation σ^{-1}). Also included is the curve of $C_{P,max}$ for an isolated plate as a function of ξ. Obviously, this last curve approaches that of a plate in the cascade when the separation is very large ($\sigma^{-1} \to \infty$; note that the curve for $\sigma^{-1} = 10$ is already quite close to that of a single plate). It is observed that $C_{P,max}$ for a plate in the cascade is larger than for an isolated plate only in a small range of values of σ close to unity, provided that ξ is also near unity.

Figure 16 depicts the angles of attack α corresponding to the $C_{P,max}$ in Fig. 15. For large ξ the values of α_{max} for a plate in the cascade are relatively small and quite similar to the values for an isolated plate, as explained above. As ξ decreases, α_{max} increases for both the cascade and the isolated plate. Note the "zigzag" behavior of the curve for the isolated plate in the low

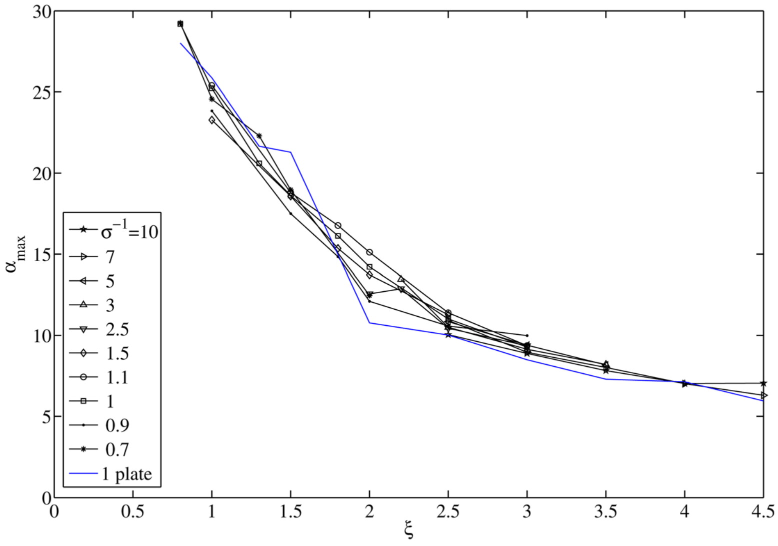

FIG. 16. Values of the angle of attack α (°) corresponding to the $C_{P,max}$ in Fig. 15.

ξ region, which is due to the fact that α_{max} is within the stalled region for a single plate. The cascade results in Fig. 16 are almost independent of σ and can be approximated by the relation $\alpha_{max} \simeq 24.874\,\xi^{-0.876}$.

The results in Fig. 15 show that $C_{P,max}$ increases as σ decreases (the separation between plates increases) and ξ increases, approaching the values for an isolated plate as $\sigma^{-1} \to \infty$. However, $C_{P,max}$ is not very appropriate for selecting the optimum values of σ and ξ because one has to take into account that the total power carried by the cascade obviously increases with the number of plates per unit length; i.e., it increases linearly with the solidity, or blade packing density, σ. For this reason, it is convenient to define a new power coefficient,

$$\bar{C}_P \equiv \sigma C_P = (C_L - \xi C_D)\xi\sqrt{1+\xi^2}\sigma, \tag{10}$$

which is proportional to the nondimensional power extracted per unit length of the cascade of plates. The maximum values of this quantity with respect to α as ξ is varied, for selected values of σ, are plotted in Fig. 17. It is clear from this figure that the optimum value of σ (yielding the highest values of $\bar{C}_{P,max}$) is close to unity. This can be explained as a compromise between small values of σ, for which $C_{P,max}$ is larger but the blade packing density is smaller, and high values of σ, for which the proximity between blades diminishes the lift coefficient of each blade, as we have seen above. Within $\sigma \approx 1$, the optimum performance is reached for ξ between 2 and 2.5. However, these values of ξ are perhaps too large for practical interest, and one may select the other relative maximum observed in Fig. 17 for $\sigma = 1$ around $\xi = 1.5$. All this is better appreciated in Fig. 18, where the maximum values of $\bar{C}_P$ are potted in a contour map in the plane (σ^{-1}, ξ) by interpolating the curves shown in Fig. 17. The top value of $\bar{C}_P$ is reached for σ between 0.9 and unity when ξ is between 2 and 2.5. However, there is another relative maximum, also with σ close to unity, when $\xi \approx 1.5$, which is probably preferred because $\xi \gtrsim 2$ might not be attained from a practical point of view. These two maxima of $\bar{C}_P$ for $\sigma \approx 1$ are related to the shift discussed above from small optimum angle of attack α_{max}, when ξ is large and the drag coefficient is more relevant for $\bar{C}_P$, to higher values of α_{max} when ξ diminishes (see Figs. 12 and 11, respectively). In any case, this figure tells us that the best operating conditions are in a broad region with σ between 0.8 and unity and ξ between 1.5 and 2.5, approximately.

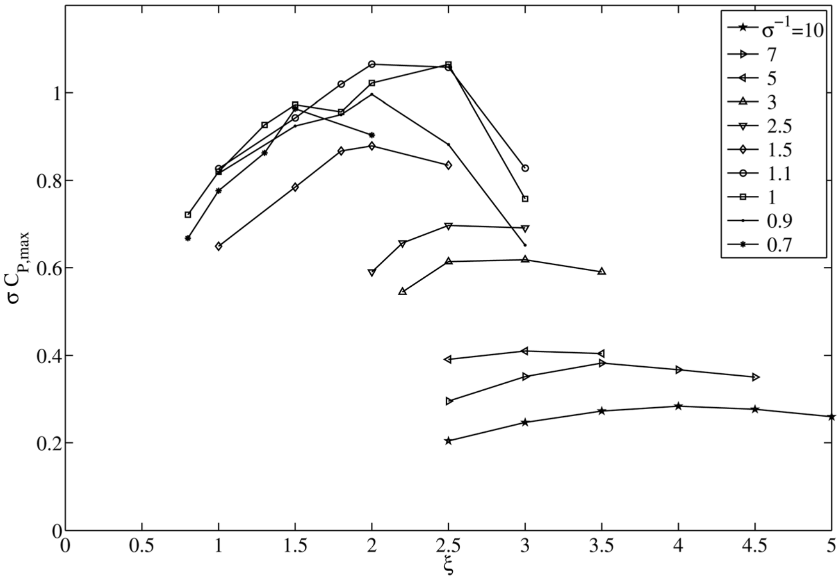

FIG. 17. $\bar{C}_{P,max} \equiv \sigma C_{P,max}$ as a function of ξ for different σ.

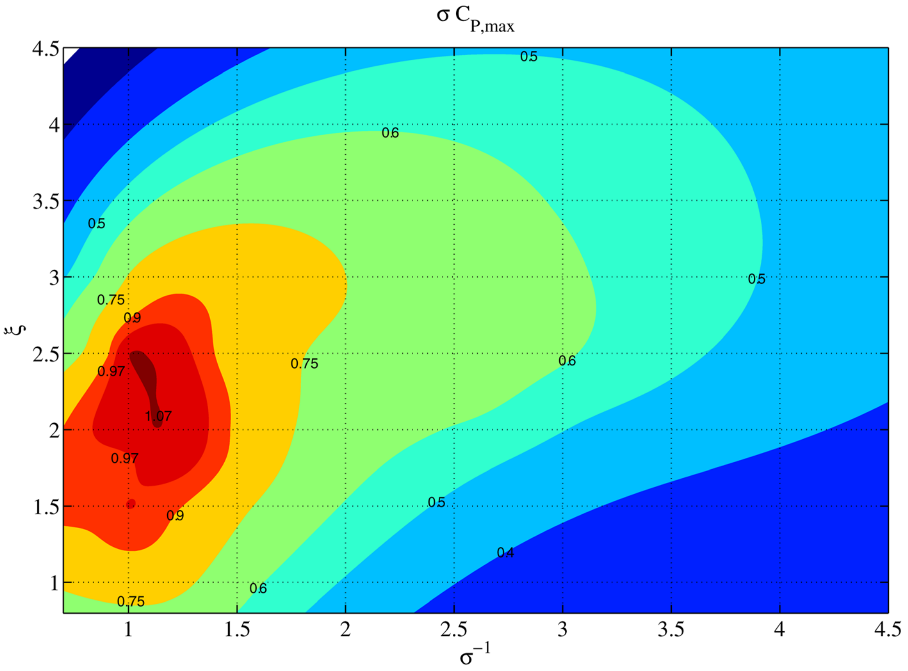

FIG. 18. Contour plot of $\bar{C}_{P,max}$ in the (σ^{-1}, ξ)-plane.

To find out the optimum values of the stagger angle $\gamma = \alpha + \theta$ of the plates corresponding to these top values of $\bar{C}_P$, Fig. 19 shows the contour map of γ_{max} in the plane (σ^{-1}, ξ) corresponding to the maximum of $\bar{C}_P$ depicted in Fig. 18. Remember that $\theta = \arctan(\xi)$, so that γ_{max} basically increases with ξ, except for the additional variation of α_{max} with ξ and σ (Fig. 16). For $\sigma \approx 1$ and $\xi \approx 2.5$ the optimum value is $\gamma_{max} \approx 79°$, while for $\xi \approx 1.5$, $\gamma_{max} \approx 75°$. Note

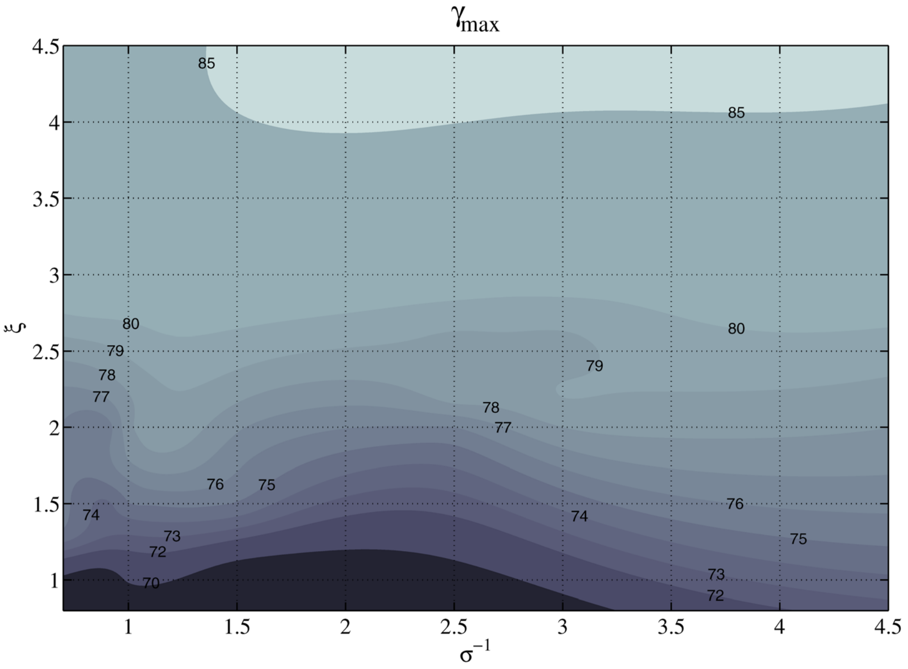

FIG. 19. Contour plot of $\gamma_{max}(°)$ in the (σ^{-1}, ξ)-plane corresponding to $\bar{C}_{P,max}$ in Fig. 18.

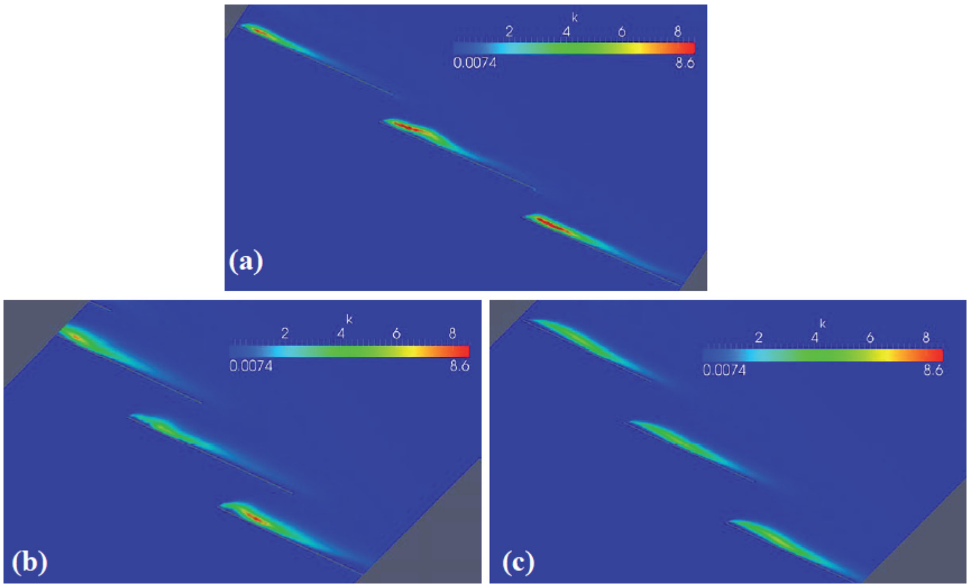

FIG. 20. Plan view of the computed turbulence kinetic energy k (m^2/s^2) on a portion of the middle plane $z = 1.5c$ for the final steady state of the 3D flow through a cascade with $\sigma = 1$, $\xi = 1.5$ and $\alpha = 35^\circ$ (a), $\sigma = 1.43$, $\xi = 1$ and $\alpha = 25^\circ$ (b), and $\sigma = 1$, $\xi = 1$ and $\alpha = 25^\circ$ (c). (sAR = 3, $Re_W = 8 \times 10^4$, $k_\infty = 0.0074\,\mathrm{m}^2/\mathrm{s}^2$.)

that the decrease in α_{max} as ξ increases commented on above is more than compensated by the increase of θ with ξ, resulting in a similar value of γ_{max} for both optimum values of ξ.

It is interesting to plot the distribution of turbulence kinetic energy for the case of maximum power, and compare it with some other configurations, since it yields useful information about the intensity of the vortices and it has been shown in wind turbines that its vertical flux is of the same order of magnitude as the power extracted by the wind turbines.[18] It is seen in Fig. 20 that the turbulent kinetic energy is highly concentrated above the leading edge of the blades,[7] and it is slightly larger in the case where a relative maximum of the power coefficient is reached (for $\xi = 1.5$ and $\sigma = 1$) than in the other two cases for which the power coefficient is smaller ($\xi = 1$ and two different values of σ; note that Figs. 20(b) and 20(c) correspond to the same cases plotted in Figs. 14 and 7, respectively).

V. CONCLUSIONS

In this study, we have performed a series of detailed CFD simulations with the objective of finding out the optimum hydrodynamic configuration of a particular device for extracting energy from tidal or river currents,[4] using a simplified model of the device consisting of a cascade of flat plates moving perpendicularly to the current. The nondimensional parameters which have been varied in the present study are the angle of the blades (stagger angle γ in relation to the tidal current), the separation between blades (solidity $\sigma = c/s$) and the blades speed ($\xi = U/V$), while the Reynolds number Re of the tidal current and the semispan aspect ratio (sAR) of the blades have been kept constant. We have chosen values of Re and sAR which are in the range of interest for the tidal energy device under consideration, and for which there exists reliable experimental data for a single plate to validate the numerical simulations. Thus we selected the turbulence model and the values of their upstream turbulent parameters that best fitted these experimental results, in addition to the optimum number of mesh cells for the computations in each case.

For the particular configuration selected that moves perpendicularly to the tidal current, and for flat plates with the given aspect ratio and selected Reynolds number, we find that optimal results (maximum power coefficient per unit length of the cascade $\bar{C}_P$) are obtained when the solidity $\sigma \approx 1$, the stagger angle $\gamma \approx 79^\circ$ and the blades speed, related to the the tidal current, $\xi \approx 2.5$. A second best configuration, with a relative maximum value of $\bar{C}_P$ slightly smaller, is $\sigma \approx 1$, $\gamma \approx 75^\circ$ and $\xi \approx 1.5$. This last configuration is preferred because its smaller value of ξ would be more easily obtained from a practical point of view. In either case, the optimum solidity is about unity and the best stagger angle around 75°.

Although the hydrodynamic performance of the device will obviously improve if airfoils with more sophisticated profiles than a simple flat plate were used in the cascade, we believe that the present aerodynamic study fulfills the basic objective of finding out a first approximation for the optimal cascade configurations in terms of γ, σ, and ξ. Further studies, both experimental and computational, using blades with different profiles and aspect ratios, and moving in a cascade at different angles in relation to the tidal current, with different Reynolds numbers, are needed to refine the optimal configurations here obtained, which may be used as starting points.

ACKNOWLEDGMENTS

This work has been supported by the Ministerio de Ciencia e Innovación of Spain, Grant No. ENE2010-16851. Comments by Pedro Mayorga, Technical Director of EnerOcean S.L. are gratefully acknowledged.

APPENDIX: TURBULENCE MODELS

Two different turbulence models are used in this work: a RNG $k-\epsilon$ model,[11] and a SST $k-\omega$ model.[12] In the RNG $-k-\epsilon$ model, the equation for the dissipation ϵ accounts for the different scales of motion through changes to the production term, while the equation for the kinetic energy k does not differ from that of the standard $k-\epsilon$ model.[9,10] For a constant density flow,

$$\frac{\partial k}{\partial t} + \nabla \cdot (k\mathbf{v}) = \nabla \cdot \left[\left(\nu + \frac{\nu_t}{\sigma_k}\right)\nabla k\right] + P_k - \epsilon, \tag{A1}$$

$$\frac{\partial \epsilon}{\partial t} + \nabla \cdot (\epsilon\mathbf{v}) = \nabla \cdot \left[\left(\nu + \frac{\nu_t}{\sigma_\epsilon}\right)\nabla \epsilon\right] + C_{1\epsilon}\frac{\epsilon}{k}P_k - C^*_{2\epsilon}\frac{\epsilon^2}{k}\,. \tag{A2}$$

In this model, the kinematic eddy viscosity is given by

$$\nu_t = C_\mu \frac{k^2}{\epsilon}\,. \tag{A3}$$

The energy production term is

$$P_k = \nu_t S^2\,, \tag{A4}$$

with $S = \sqrt{2\mathbf{S}:\mathbf{S}}$, the modulus of the mean rate-of-strain tensor, $\mathbf{S} = [\nabla\mathbf{v} + (\nabla\mathbf{v})^T]/2$, and

$$C^*_{2\epsilon} = C_{2\epsilon} + \frac{C_\mu \eta^3(1-\eta/\eta_0)}{1+\beta\eta^3}, \qquad \eta = \frac{Sk}{\epsilon}\,. \tag{A5}$$

For the nondimensional constants in the above expressions we use the following common values, which differ from those commonly used in the standard $k-\epsilon$ model:[10,11] $C_\mu = 0.0845$, $\sigma_k = \sigma_\epsilon = 0.7194$, $C_{1\epsilon} = 1.42$, $C_{2\epsilon} = 1.68$, $\eta_0 = 4.38$, and $\beta = 0.012$.

The SST $-k-\omega$ model is directly usable all the way down to the wall through the viscous sub-layer without any extra damping functions, being more appropriate than the $k-\epsilon$ model for low Reynolds number turbulence, and is equivalent to a $k-\epsilon$ model in the free-stream, avoiding the common $k-\omega$ problem that the model is too sensitive to the inlet free-stream turbulence properties.[10,12] The maximum of the kinematic eddy viscosity, which in the standard $k-\omega$ model is given by $\nu_t = k/\omega$, is limited by forcing the turbulent shear stress to be bounded,

$$\nu_t = \frac{a_1 k}{\max(a_1 \omega, S F_2)}\,, \tag{A6}$$

where $a_1 = 0.31$ and F_2 is an auxiliary function of the wall distance y given by

$$F_2 = \tanh\left\{\left[\max\left(\frac{2\sqrt{k}}{\beta^* \omega y}\,, \frac{500\nu}{y^2\omega}\right)\right]^2\right\}. \tag{A7}$$

The equations for the turbulent kinetic energy k and the specific dissipation rate ω can be written, for a constant density flow, as

$$\frac{\partial k}{\partial t} + \nabla\cdot(k\mathbf{v}) = \nabla\cdot[(\nu + \sigma_k \nu_t)\nabla k] + P_k - \beta^* k\omega\,, \tag{A8}$$

$$\frac{\partial \omega}{\partial t} + \nabla\cdot(\omega\mathbf{v}) = \nabla\cdot[(\nu + \sigma_\omega \nu_t)\nabla \omega] + \alpha S^2 - \beta\omega^2 + 2(1-F_1)\sigma_{\omega 2}\frac{1}{\omega}\nabla k\cdot\nabla\omega\,, \tag{A9}$$

where now

$$P_k = \min(\nu_t S^2\,, 10\beta^* k\omega)\,, \tag{A10}$$

and $\beta^* = 9/100$,

$$F_1 = \tanh\left\{\left\{\min\left[\max\left(\frac{\sqrt{k}}{\beta^*\omega y}\,, \frac{500nu}{y^2\omega}\right), \frac{4\sigma_{\omega 2} k}{CD_{k\omega} y^2}\right]\right\}^4\right\}, \tag{A11}$$

$$CD_{k\omega} = \max\left(2\sigma_{\omega 2}\frac{1}{\omega}\nabla k\cdot\nabla\omega\,, 10^{-10}\right). \tag{A12}$$

If we denote any of the model coefficients β, α, σ_k, and σ_ω as ϕ, they are defined by blending the coefficients of the original $k-\omega$ model, denoted as ϕ_1, with those of the transformed $k-\epsilon$ model, denoted as ϕ_2, through

$$\phi = F_1\phi_1 + (1-F_1)\phi_2. \tag{A13}$$

The specific values of the non-dimensional parameters used here are:[12] $\alpha_1 = 5/9$, $\alpha_2 = 0.44$, $\beta_1 = 3/40$, $\beta_2 = 0.0828$, $\sigma_{k1} = 0.85$, $\sigma_{k2} = 1$, $\sigma_{\omega 1} = 0.5$, and $\sigma_{\omega 2} = 0.856$.

In Sec. III we selected the upstream values of k, ϵ and ω for each model that best fit the experimental data for an isolated plate, but we used the common values of the turbulence model constants given above.

In relation to the boundary conditions on the plate walls, we used several standard wall functions (see, e.g., Ref. 19) implemented in the OPENFOAM toolbox. In particular, these boundary conditions are applied at a distance to the wall $y = y_p$ in the log-law region where y^+ is around 50, where $y^+ \equiv y/(\nu/u_*)$ is the distance to the wall in wall units. They are

$$\left.\frac{\partial k}{\partial y}\right|_{y=y_p} = 0\,, \quad \epsilon = \epsilon_p = \frac{C_\mu^{3/4} k_p^{3/2}}{\kappa y_p}\,, \quad \omega = \omega_p = \sqrt{\omega_{vis}^2 + \omega_{log}^2}\,, \tag{A14}$$

$$\omega_{vis} = \frac{6\nu}{\beta y_p^2}\,, \quad \omega_{log} = \frac{k_p^{1/2}}{C_\mu^{1/4}\kappa y_p}\,, \tag{A15}$$

with $k_p = k$ at $y = y_p$, and $\kappa = 0.41$ the von Kármán constant. In our computations with the medium mesh (e.g., case 6 in Table I), the minimum value of y^+ was 0.1 and its medium value for the wall grid cells was 3.1. The corresponding minimum cell area in a constant z plane was $3.1 \times 10^{-6}\, c^2$, where c is the chord length.

[1] M. J. Khan, G. Bhuyan, M. T. Iqbal, and J. E. Quaicoe, "Hydrokinetic energy conversion systems and assessment of horizontal and vertical axis turbines for river and tidal applications: A technological status review," Appl. Energy **86**, 1823–1835 (2009).
[2] F. O Rourke, F. Boyle, and A. Reynolds, "Tidal energy update 2009," Appl. Energy **87**, 398–409 (2010).
[3] R. H. Charlier and C. W. Finkl, *Ocean Energy. Tide and Tidal Power* (Springer, Berlin, 2009).
[4] See http://tidalsails.com for "Tidal Sails AS," 2012.
[5] W. M. J. Batten, A. S. Bahaj, A. F. Molland, and J. R. Chaplin, "The prediction of the hydrodynamic performance of marine current turbines," Renewable Energy **33**, 1085–1096 (2008).
[6] I. S. Hwang, Y. H. Lee, and S. J. Kim, "Optimization of cycliodal water turbine and the performance improvement by individual blade control," Appl. Energy **86**, 1532–1540 (2009).
[7] S. S. Mukherji, N. Kolekar, A. Banerjee, and R. Mishra, "Numerical investigation and evaluation of optimum hydrodynamic performance of a horizontal axis hydrokinetic turbine," J. Renewable Sustainable Energy **3**, 063105 (2011).
[8] See http://www.openfoam.com for "OpenFOAM," 2012.
[9] W. Rodi, *Turbulence Models and Their Application in Hydraulics. A State-of-the-art Review*, 3rd ed. (Balkema, Rotterdam, 2000).
[10] T. Cebeci, *Turbulence Models and Their Application* (Springer–Verlag, Berlin, 2004).
[11] V. Yakhot, S. A. Orszag, S. Thangam, T. B. Gatski, and C. G. Speziale, "Development of turbulence models for shear flows by a double expansion technique," Phys. Fluids A **4**, 1510–1520 (1992).
[12] F. R. Menter, "Two-equation eddy-viscosity turbulence models for engineering applications," AIAA J. **32**, 1598–1605 (1994).
[13] A. Pelletier and T. J. Mueller, "Low Reynolds number aerodynamics of low-aspect-ratio, thin/flat/cambered-plate wings," J. Aircr. **37**, 825–832 (2000).
[14] Y. Saad, *Iterative Methods for Sparse Linear Systems*, 2nd ed. (SIAM, Philadelphia, 2003).
[15] L. F. Richardson, "The approximate arithmetical solution by finite differences of physical problems involving differential equations with an application to the stresses in a masonry dam," Philos. Trans. R. Soc. London **210**, 307–357 (1910).
[16] P. J. Roache, *Verification and Validation in Computational Science and Engineering* (Hermosa Publishers, Albuquerque, 1998).
[17] F. S. Weinig, "Theory of two-dimensional flow through cascades," in *Aerodynamics of Turbines and Compressors*, edited by W. R. Hawthorne, High Speed Aerodynamics and Jet Propulsion Vol. 10 (Princeton University Press, Cambridge, USA, 1964), pp. 13–81.
[18] R. B. Cal, J. Lebrón, L. Castillo, H. S. Kang, and C. Meneveau, "Experimental study of the horizontally averaged flow structure in a model wind-turbine array boundary layer," J. Renewable Sustainable Energy **2**, 013106 (2010).
[19] S. B. Pope, *Turbulent Flows* (Cambridge University Press, 2000).